

Atomic-layer controlled THz Spintronic emission from Epitaxially grown Two dimensional PtSe₂/ferromagnet heterostructures

K. Abdukayumov,^{1,*} M. Mičica,^{2,*} F. Ibrahim,¹ C. Vergnaud,¹ A. Marty,¹ J.-Y. Veuillen,³ P. Mallet,³ I. de Moraes,¹ D. Dosenovic,⁴ Adrien Wright,² Jérôme Tignon,² Juliette Mangeney,² A. Ouerghi,⁵ V. Renard,⁶ F. Mesple,⁶ F. Bonell,¹ H. Okuno,⁴ M. Chshiev,¹ J.-M. George,⁷ H. Jaffrès,⁷ S. Dhillon,² and M. Jamet¹

¹*Univ. Grenoble Alpes, CEA, CNRS, Grenoble INP, IRIG-Spintec, 38000 Grenoble, France*

²*Laboratoire de Physique de l'Ecole Normale Supérieure, ENS, Université PSL, CNRS, Sorbonne Université, Université de Paris, Paris, France*

³*Université Grenoble Alpes, CNRS, Grenoble INP, Institut NEEL, 38000 Grenoble, France*

⁴*Université Grenoble Alpes, CEA, IRIG-MEM, 38000 Grenoble, France*

⁵*Université Paris-Saclay, CNRS, Centre de Nanosciences et de Nanotechnologies, 91120, Palaiseau, France*

⁶*Université Grenoble Alpes, CEA, CNRS, IRIG-PHELIQS, 38000 Grenoble, France*

⁷*Unité Mixte de Physique, CNRS, Thales, Université Paris-Saclay, F-91767 Palaiseau, France*

(Dated: May 12, 2023)

Abstract

Terahertz (THz) Spintronic emitters based on ferromagnetic/metal junctions have become an important technology for the THz range, offering powerful and ultra-large spectral bandwidths. These developments have driven recent investigations of two-dimensional (2D) materials for new THz spintronic concepts. 2D materials, such as transition metal dichalcogenides (TMDs), are ideal platforms for SCC as they possess strong spin-orbit coupling (SOC) and reduced crystal symmetries. Moreover, SCC and the resulting THz emission can be tuned with the number of layers, electric field or strain. Here, epitaxially grown 1T-PtSe₂ and sputtered Ferromagnet (FM) heterostructures are presented as a novel THz emitter where the 1T crystal symmetry and strong SOC favor SCC. High quality of as-grown PtSe₂ layers is demonstrated and further FM deposition leaves the PtSe₂ unaffected, as evidenced with extensive characterization. Through this atomic growth control, the unique thickness dependent electronic structure of PtSe₂ allows the control of the THz emission by SCC. Indeed, we demonstrate the transition from the inverse Rashba-Edelstein effect in one monolayer to the inverse spin Hall effect in multilayers. This band structure flexibility makes PtSe₂ an ideal candidate as a THz spintronic 2D material and to explore the underlying mechanisms and engineering of the SCC for THz emission.

I. INTRODUCTION

During the past two decades, two-dimensional (2D) materials have raised tremendous interest in the scientific community for the novel and specific properties as a result of their reduced dimensionality and van der Waals character [1–3]. In particular, when isolated to one monolayer (ML), transition metal dichalcogenides (TMD) 1H-MX₂ (with M=Mo, W and X=S, Se) become direct bandgap semiconductors with remarkable optical properties [4, 5]. In addition, inversion symmetry breaking giving rise to in-plane electric field combined with strong spin-orbit coupling gives rise to two inequivalent K valleys exhibiting spin-valley locking [6]. This property is at the origin of unique phenomena such as optical valley selection by circularly polarized light [7], large valley Hall and Nernst effects [8, 9], anisotropic spin relaxation [10] and sizeable spin-orbit torques [11]. Platinum diselenide (PtSe₂) is a recent TMD that shows several key properties like air stability [12], high carrier mobility [13], high

* These two authors equally contributed to the present work.

photoelectrical response in the near-infrared range [14] and defect-induced ferromagnetism [15]. By selectively substituting selenium by sulfur atoms, the polar SePtS Janus material could also be synthesized [16]. Moreover, it exhibits a layer-dependent bandgap: one monolayer of PtSe₂ is a 1.9 eV bandgap semiconductor while for layers greater than 3 ML it becomes semi-metallic [17]. Finally, owing to the large atomic weight of platinum, PtSe₂ possesses the greatest spin-orbit coupling among transition metal diselenides making it an excellent candidate to study spin-to-charge conversion (SCC) in van der Waals materials. In this respect, it constitutes a unique system to observe the transition from inverse Rashba-Edelstein effect (IREE) in the semiconducting phase to inverse spin Hall effect (ISHE) in the semi-metallic phase. Furthermore, 1T-PtSe₂ shows crystal inversion symmetry favoring in-plane spin textures at interfaces whereas spins are mostly locked out-of-plane in 1H-MX₂ preventing SCC for in-plane polarized spin currents. Angle and spin-resolved photoemission spectroscopy measurements have indeed demonstrated the existence of in-plane helical spin textures in the valence band of monolayer PtSe₂ [18, 19]. To study SCC in 2D materials, spin pumping is typically used and has, for example, been used to measure the strength of IREE [20]. On the other hand, Terahertz (THz) emission spectroscopy has become a powerful and established tool to probe SCC [21, 22]. The associated devices are known as spintronic THz emitters and were first demonstrated with metallic ferromagnetic (Co, Fe...)/nonmagnetic (Pt, W...) thin films [23–25]. They present several advantages compared to other THz sources such as broadband THz emission, high efficiency and easy control of radiation parameters. To date, very few 2D materials have been incorporated in THz spintronic emitters [26–29] and they all exhibit the 1H crystal structure which is not favorable to convert in-plane polarized spins into charge currents. Indeed, the combination of inversion symmetry breaking and strong SOC forces the spin of electrons with finite momentum to be out-of-plane. In this work, we have grown single crystalline mono and multilayers of 1T-PtSe₂ on graphene by van der Waals epitaxy [30–33] and developed a soft sputtering process to grow amorphous CoFeB on top of PtSe₂ obtaining atomically sharp CoFeB/PtSe₂ interface. We used a full set of characterization tools to demonstrate the structural and chemical preservation of PtSe₂ after CoFeB deposition. SCC was then studied on these advanced 2D samples as a function of PtSe₂ thickness from 1 to 15 ML using THz emission spectroscopy that showed the efficient generation of THz electric fields through SCC. This THz emission is shown to arise from the 1T crystal structure and large

spin-orbit coupling of PtSe₂. Indeed, negligible signals were obtained for 1T-VSe₂ with low spin-orbit coupling and for 1H-WSe₂ with 1H crystal structure. Further, the THz electric field clearly shows a two-step dependence on the PtSe₂ thickness that we interpret as the transition from the IREE in the semiconducting regime to the ISHE in the semimetallic regime. As shown by ab initio calculations, the IREE arises from the large Rashba spin splitting at the PtSe₂/graphene interface by the combination of large spin-orbit coupling and the interfacial electric dipole. By fitting the thickness dependence, we could extract the out-of-plane spin diffusion length in PtSe₂ to be 2-3 nm and found that SCC by IREE at the PtSe₂/Gr interface is twice as efficient than that of ISHE in bulk PtSe₂. For its unique thickness dependent electronic structure, PtSe₂ spintronic structures enable to observe the transition from IREE to ISHE and opens up perspectives for the application of these structures to THz spintronics. Furthermore, by adjusting the Fermi level position via gating the material, it will be possible to modulate and dramatically enhance the SCC efficiency and achieve further large enhancement of the spintronic THz emission.

II. RESULTS AND DISCUSSION

A. Sample growth and characterization

All the samples are grown under ultra-high vacuum (UHV) conditions in the low 10^{-10} mbar pressure range. Substrates are epitaxial graphene on undoped SiC(0001) thermally prepared by surface graphitization [34, 35]. The low spin-orbit interaction in graphene and SiC ensures negligible SCC. Prior to the growth, the substrates are annealed at 800°C during 30 minutes under UHV to desorb contaminants. The substrate is then maintained at 300°C during the growth. Platinum is evaporated using an electron gun at a constant rate of 0.003125 Å/s for 1 ML PtSe₂ and 0.00625 Å/s for the other thicknesses as monitored by a quartz microbalance. Selenium is evaporated using a Knudsen cell with a vapor pressure of 10^{-6} mbar at the sample position. This ensures a large Se:Pt ratio greater than 10 necessary to avoid the formation of Se vacancies in the material. Up to 3 ML of PtSe₂, the growth is performed in this one step whilst for thicker films, it is achieved in several steps alternating deposition and annealing at 700°C under Se to smooth out the surface. At the end of the growth, all the films are annealed at 700°C during 15 minutes to improve the crystal quality.

PtSe₂ grows epitaxially on graphene and typical reflection high energy electron diffraction patterns (RHEED) are shown in Fig. 1a along two azimuths 30° apart from each other. The observed thin streaks and anisotropic character demonstrate the high crystalline quality of PtSe₂ films, *i.e.* large grain size and good crystalline orientation. As usually observed in van der Waals epitaxy of 2D materials on graphene, the mosaic spread measured by azimuthal in-plane x-ray diffraction shows a maximum of $\pm 5^\circ$ [30]. Thanks to the air stability of PtSe₂, it is possible to perform ex-situ characterization. The Raman spectrum (see Experimental section) for 10 ML of PtSe₂ is shown in Fig. 1b. We clearly distinguish the two characteristic vibration modes of PtSe₂ E_g (in-plane) at 177.9 cm⁻¹ and A_{1g} (out-of-plane) at 206.9 cm⁻¹ with typical full width at half maximum (FWHM) of 4 cm⁻¹ [36]. Atomic force microscopy (AFM) images performed on less than 1 and 3 ML are shown in Fig. 1c and 1d, respectively. For partially covered graphene in Fig. 1c, the height profile gives identical PtSe₂/Gr and PtSe₂/PtSe₂ step heights of ≈ 0.5 nm corresponding to the c-lattice parameter of bulk PtSe₂. Moreover, for 3 ML in Fig. 1d, the AFM image illustrates the quasi completion (96.6 %) of the third layer and the layer-by-layer film growth. This growth mode allows for the fine control of the number of deposited PtSe₂ monolayers.

Scanning tunnelling microscopy (STM) and spectroscopy (STS) measurements were made on a sample grown on bilayer graphene (BLG). The nominal thickness of the PtSe₂ film was 1 ML. As shown in Fig. 1e, the sample consists mostly of the monolayer (1 ML) PtSe₂, with small islands of bilayer PtSe₂ (2 ML) and patches of the bare BLG substrate. The lateral size of the 1 ML islands is in the ten nanometers range. Fig. 1e is a medium scale STM image of an area with different semiconducting objects: a few connected 1 ML PtSe₂ grains and a 2 ML island. Larger scale STM image and height distribution are shown in the Supp. Information. Fig. 1f displays spectra taken on two 1 ML grains. The curves are quite similar (this also holds for the spectra taken on the other grains), and reveal a gap estimated to be 1.93 eV. The Fermi level E_F (corresponding to zero sample bias) is close to the conduction band minimum (CBM), located at +0.25 V, whereas the valence band maximum (VBM) is found to be -1.68 eV below E_F. From a series of measurements on 1 ML islands on a BLG substrate we find an average gap width of 1.95 ± 0.05 eV, with a CBM (VBM) located 0.24 ± 0.03 eV above (1.70 ± 0.05 eV below) the Fermi level. This gap value is similar to the ones reported in previous papers for 1 ML PtSe₂ grown on Highly Ordered Pyrolytic Graphite (HOPG), which ranged from 1.8 eV [37] to 2.00 ± 0.10 eV [38] and 2.09 eV [39].

In these reports, the CBM of the 1 ML PtSe₂ on HOPG substrate is located typically 0.55 eV above the Fermi level, a value larger than the one we find here for a BLG substrate. This shift of the CBM is consistent with the difference in the work functions of BLG and HOPG, which amounts to approximately 0.20 eV [40], as expected for a weak Fermi level pinning at the graphene/TMD interface [41]. Following the same argument, the CBM of 1 ML PtSe₂ grown on monolayer graphene on SiC(0001) as the one used for THz emission should be located between 100 and 150 meV above the Fermi level. It results from the decrease by 100 meV [40] to 135 meV [42] of the substrate work function between monolayer and bilayer graphene on SiC(0001). This statement is supported by experimental data for other semiconducting TMD grown on epitaxial graphene [43].

We conclude that the Fermi level of 1 ML PtSe₂ is systematically shifted towards the CBM as a consequence of electron transfer from graphene to PtSe₂ [30, 44]. This charge transfer is discussed later from the theoretical point of view and for its consequence on SCC. Finally, in-plane and out-of-plane x-ray diffraction (see Experimental section) on 6 ML PtSe₂ (not shown) yield the following lattice parameters: $a=3.703 \text{ \AA}$ and $c=5.14 \text{ \AA}$. It corresponds to an in-plane compression of -0.6 % and out-of-plane expansion of +1.1 % with respect to bulk PtSe₂ [45]. The full width at half maximum (FWHM) of (100) and (110) Bragg peaks are 0.57° and 0.61° , respectively, close to the instrumental resolution. It reveals the large grain size of the PtSe₂ film.

Next, in order to perform THz spintronic emission, we deposit 3 nm of amorphous CoFeB on top of PtSe₂ covered by 4 nm of aluminum that transforms into AlO_x to protect the ferromagnetic layer against oxidation. We use soft sputtering conditions for CoFeB deposition not to damage the PtSe₂ surface. We set the argon pressure to 1.25×10^{-2} mbar and the deposition rates are 0.319 \AA/s for CoFeB and 0.265 \AA/s for Al respectively. Moreover, the MBE evaporation chamber being connected to the magnetron sputtering reactor, all PtSe₂ films are transferred in-situ under UHV conditions fully preserving the PtSe₂ surface from contamination. In Fig. 2, we used a full set of characterization tools to study the impact of CoFeB deposition on PtSe₂ properties. In Fig. 2a, all the Raman spectra for 1-18 ML of PtSe₂ exhibit the two same E_g and A_{1g} vibration modes demonstrating that the TMD film retains its crystal integrity after CoFeB deposition. For 10 ML of PtSe₂, E_g and A_{1g} peaks fall exactly at the same positions with and without CoFeB. We observe an increase of the E_g/A_{1g} intensity ratio when increasing the thickness as already observed for pristine PtSe₂

[19]. This result is confirmed by in-plane and out-of-plane x-ray diffraction as shown in Fig. 2b and 2c for 5 ML and 15 ML of PtSe₂, respectively. First, the radial scans along the reciprocal directions at 0° and 30° of the substrate SiC(hh0) directions show the diffraction peaks of the substrate and PtSe₂. The anisotropic character indicates that the layers are crystallographically well oriented in epitaxy with respect to the substrate. From the Bragg peak positions, we obtain the in-plane and out-of-plane lattice parameters: a=3.709 Å (resp. a=3.713 Å) and c=5.18 Å (resp. c=5.14 Å) for 5 ML (resp. 15 ML). They perfectly match the values obtained on 6 ML of PtSe₂ without CoFeB. Moreover, the FWHM of in-plane (100) and (110) Bragg peaks (0.55°, 0.63° for 5 ML and 0.42°, 0.57° for 15 ML) are comparable to that of PtSe₂ without CoFeB and confirms the large grain size. In addition, from the diffraction fringes around (001) Bragg peaks, we can conclude that the CoFeB/PtSe₂ interface is flat at the atomic scale and deduce the film thickness to be 2.4 nm (2.5 nm expected) for 5 ML and 7.0 nm (expected 7.5 nm) for 15 ML.

These results confirm that PtSe₂ films are not affected by the deposition of CoFeB. The interface atomic structure and chemical composition are further investigated by scanning transmission electron microscopy (STEM) in the high angular annular dark field (HAADF) mode and in situ x-ray photoemission spectroscopy (XPS) respectively. Fig. 2d shows in the dark and bright field modes 8 ML of PtSe₂ epitaxially grown on Gr/SiC and covered by CoFeB. We clearly distinguish an atomically sharp interface with a 0.7 nm gap between the PtSe₂ and CoFeB. In Fig. 2e and 2f, XPS spectra of Pt 4f and Se 3d core levels are recorded on 3 ML of PtSe₂ before and after deposition of 1 nm of CoFeB. For both elements, the spectra superimpose before and after CoFeB deposition while the signal decrease after CoFeB deposition is due to the partial absorption of photoelectrons by the metallic film. To summarize, we can conclude from TEM and XPS analysis that the PtSe₂ surface is preserved after CoFeB deposition.

B. THz spintronic emission

Measurements of the emitted THz waves from CoFeB/TMD samples are performed using THz emission time domain spectroscopy (TDS) as depicted in Fig. 3a. The sample is placed in a magnetic mount to apply an in-plane magnetic field of approximately 20 mT, with independent rotation of the sample and magnetic field. It is excited by a Ti:Sapphire

oscillator (Coherent MIRA, 15-100 fs pulse length and horizontal polarization) at a wavelength of 800 nm in the near infrared (NIR) range. The average power exciting the sample is about 300 mW (after modulation by a chopper), adjustable by a half-wave plate followed by a polarizer. The emitted radiation is collected by a system of parabolic mirrors and the residual NIR pump is filtered by a Teflon plate. The last parabolic mirror with a hole in the center superimposes the emitted THz and the probe NIR pulse and focuses the THz beam on a ZnTe crystal for electro-optic detection with sensitivity set to horizontal component of the THz electric field (E-field). The ultrashort femtosecond laser pulse excites spin polarized electron-hole pairs in the ferromagnet (CoFeB) creating a net spin accumulation that generates a spin current into the non-magnetic layer (here the TMD) to be converted into a transverse charge current by ultrafast SCC. This results in an emitted electromagnetic pulse with frequencies in the THz range. As shown in Fig. 3b, we use both transmission (from the front and back sides) and reflection modes, which are used to show the spintronic origins of the THz emission. In Fig. 4a, we first compare spintronic THz emission from different samples: Gr/SiC bare substrate, CoFeB/Gr/SiC reference sample, CoFeB/VSe₂, CoFeB/WSe₂ and CoFeB/PtSe₂. VSe₂, WSe₂ and PtSe₂ are all 10 ML-thick. The epitaxial growth of VSe₂ and WSe₂ on graphene are detailed in [33] and [46], respectively. First, we clearly see that only CoFeB/PtSe₂ gives an enhanced THz signal with respect to the reference sample. Moreover, the Gr/SiC substrate adds no background signal. Next, CoFeB/VSe₂, CoFeB/WSe₂ and the reference sample exhibit the same THz emitted signal in sign and amplitude. We thus conclude that the origin of SCC is the same in all three samples. The common feature between the three samples being the AlO_x/CoFeB interface, we believe that the THz signal comes from the SCC at this interface through the inverse Rashba-Edelstein mechanism and/or from the self-emission of CoFeB due to unbalanced spin-flips at both interfaces. It also demonstrates that SCC in Gr/SiC, VSe₂ and WSe₂ is negligible. This can be justified by the low spin-orbit coupling of Gr/SiC and 1T-VSe₂ whereas spin-valley locking favors out-of-plane spin polarization in 2H-WSe₂ which partially prevents SCC when in-plane spins are injected. By looking at the first E-field maximum of each sample (indicated by arrows in Fig. 4a), we notice that it is opposite for PtSe₂ pointing out another SCC mechanism taking place in PtSe₂, opposite to the Rashba-Edelstein effect at the AlO_x/CoFeB interface. In the following, we focus on THz spintronic emission from PtSe₂. In Fig. 4b, we first compare the THz signals for pure Pt (5 nm) and PtSe₂ (10 ML, 5

nm) with the magnetic field applied in the same direction (B+). The SCC in Pt and PtSe₂ have the same sign and the magnitude is 7 times higher in Pt. Then, to verify the magnetic character of THz emission, we apply the magnetic field in two opposite directions (B+ and B-) and record the THz E-field in transmission mode by optically pumping the sample from the front and the back sides as shown in Fig. 4c. The opposite signs for B+ and B- and between front and back side pumping indicate the magnetic nature of the emission due to SCC in PtSe₂. The overall signal being less when pumping from the front side, it proves that SiC partially absorbs THz waves. Finally, in Fig. 4d, we plot the Fourier transform of the 4 spectra shown in Fig. 4c and find the same broad band emission in the 0-4 THz range which is comparable to other THz spintronic emitters [47]. In order to study the influence of the ferromagnetic layer and deposition technique on THz emission, we performed the same measurements using 3 nm of cobalt deposited in situ on 10 ML of PtSe₂ by electron beam evaporation (see Supp. Info.). We find very similar results showing that the ferromagnetic layer and deposition method have almost no influence on THz emission from PtSe₂.

We then study the magnetic field angle (θ) dependence in the geometry shown in Fig. 5a where a horizontal linear polarizer is introduced between the sample and the detector. Along a full 0°-360° rotation as shown in Fig. 5b, we obtain a typical $\cos(\theta)$ emission pattern with a phase reversal for opposite magnetic field directions (B+ at 0° and B- at 180°) which is a clear experimental evidence of SCC process in PtSe₂. No sizeable asymmetry in the emission lobes is observed meaning that non-magnetic contributions to the THz signal are negligible in this material. Regarding the sample angle (ϕ) dependence in Fig. 5c, we observe an isotropic signal with respect to the azimuthal crystalline orientation as expected for SCC like ISHE or IREE [48]. Moreover, the linear dependence of the THz signal $(E_{B+} + E_{B-})/2$ on the laser pump power in Fig. 5d is another experimental evidence of SCC in PtSe₂.

C. SCC mechanism in PtSe₂

In order to study the origin of SCC in PtSe₂, we performed thickness dependent measurements as shown in Fig. 5e. For this, we pumped the magnetic layer from the backside and measured the THz signal in transmission mode. We took into account the absorption of the laser and THz waves by PtSe₂ to normalize the signal (see Supp. Info.). The curve exhibits a two-step behavior that we interpret as IREE for thin PtSe₂ coverage (first step)

and ISHE for thicker PtSe₂ (second step). Indeed, the second step appears at the semiconductor (SC) to semimetallic (SM) transition of PtSe₂ as given by electrical van der Pauw measurements (see Supp. Info.). This is illustrated in Fig. 5f and 5g respectively where we assume that IREE takes place in the PtSe₂ monolayer in contact with graphene and ISHE in the semi metallic bulk PtSe₂. Based on these assumptions, we use a simple spin diffusion model to fit the experimental data. First, we assume that the spin current generated by optical excitation in CoFeB is completely absorbed in PtSe₂ (spin sink model). We denote d_N , l_{sf} , j_{s0} , θ_N and θ_I as the PtSe₂ thickness, spin diffusion length in PtSe₂, the spin current at the CoFeB/PtSe₂ interface, the spin Hall angle of PtSe₂ and effective spin Hall angle at the PtSe₂/Gr interface, respectively. We use the following equations:

$$\begin{aligned} j_s(z)/j_s(0) &= \exp(-z/l_{sf}) \\ J_N(d_N)/j_s(0) &= \int_0^{d_N} j_s(z)/j_s(0) dz = l_{sf}(1 - \exp(-d_N/l_{sf})) \end{aligned} \quad (1)$$

to describe the spin current $j_s(z)$ at a depth z from the CoFeB/PtSe₂ interface and the layer-integrated spin current in PtSe₂ $J_N(d_N)$. The profile of $j_s(z)$ is depicted in Fig. 5f and 5g. The total charge current generated by IREE and ISHE can be written as: $I_c = H(z - d_N^I)\theta_I j_s(d_N)d_N^I + H(z - d_N^C)\theta_N J_N(d_N)$ where H is a step function and d_N^I (resp. d_N^C) the PtSe₂ thickness for which IREE (resp. ISHE) sets in. The Rashba-Edelstein length is then defined as: $\lambda_{IREE} = \theta_I d_N^I$ and we assume θ_I to be independent of d_N . The best fit to the experimental data gives the following parameters: $d_N^I=0.35$ nm; $d_N^C=1.7$ nm; l_{sf} between 2 nm (green fitting curve in Fig. 5e) and 3 nm (grey fitting curve in Fig. 5e) and $\theta_I/\theta_N \approx 2$. d_N^I is comparable to 1 ML of PtSe₂ (0.27 nm) in agreement with IREE and d_N^C corresponds to 3-4 ML of PtSe₂ at the transition from semiconductor to semimetal in good agreement with ISHE. We find a short spin diffusion length between 2 nm (4 ML) and 3 nm (6 ML). The equivalent platinum thickness (corresponding to the Pt amount in 2 nm and 3 nm of PtSe₂) is between 0.65 nm and 0.975 nm demonstrating that the spin flip rate with flow along the normal to the film plane is larger in PtSe₂ than in Pt. This finding raises the question of spin diffusion with flow along the normal in lamellar systems. In particular, the role of van der Waals gaps needs to be taken into account. The short spin diffusion length could be explained if vdW gaps act as effective tunnel barriers in spin transport: during the tunnelling time between two PtSe₂ layers, in-plane spin flips occur within individual

PtSe₂ layers limiting the vertical spin transport. This would deserve further investigation and the development of a more general theory which is out of the scope of the present work. Finally, we find that IREE and ISHE have the same sign and IREE is twice more efficient than ISHE. To support our conclusions and understand the mechanisms responsible for the THz spintronic emission, we have performed first principles calculations based on the projector-augmented wave (PAW) method [49] as implemented in the VASP package [50–52] using the generalized gradient approximation [53] and including spin-orbit coupling. The PtSe₂/Gr heterostructure was constructed by matching 2×2 supercell of 1T-PtSe₂ with 3×3 supercell of graphene on top so that to minimize the lattice mismatch to less than 1.5 %. A sufficient vacuum layer of 20 Å thickness was added to the heterostructure. The atomic coordinates were relaxed until the forces became smaller than 1 meV/Å. A kinetic energy cutoff of 550 eV has been used for the plane-wave basis set and a Γ -centered 15×15×1 k-mesh was used to sample the first Brillouin zone. To describe correctly the interaction across the interface, van der Waals forces were used with Grimme type dispersion-corrected density functional theory-D2 [54]. The two-dimensional spin textures were calculated for a 10×10 Γ -centered 2D k-mesh and the PyProcar package [55] was used to plot them. In Fig. 6a and 6d, we compare the calculated band structures for a freestanding PtSe₂ and that of monolayer-PtSe₂/Gr heterostructure. The relaxed interlayer distance between PtSe₂ and Gr is found to be 3.29 Å which induces charge transfer across the interface depicted by the charge clouds in the inset of Fig. 6d. We estimate a charge transfer of about 0.04 e transferred from the graphene to the PtSe₂; a relatively small value that is consistent with the weak vdW interaction type. This is also reflected through the preserved band structure features of pristine graphene and PtSe₂ in the heterostructure which is consistent with previous theoretical reports [56]. To assess the potential Rashba effect at PtSe₂/Gr interface, the calculated spin textures for monolayer PtSe₂ and PtSe₂/Gr heterostructure are compared. Two representative bands are chosen: one in the conduction band (CB) and the other in the valence (VB) that are highlighted in blue and red in Fig. 6a, respectively. The corresponding two-dimensional spin textures displayed for the CB (VB) in Fig. 6b and 6c, show two contours with opposite spin helicities, however, they are degenerate with no splitting. This is implicit since there is no source of inversion symmetry breaking in a freestanding PtSe₂ monolayer. In this respect, the spin textures observed in Refs.[18, 19] can only be explained by the presence of an interface electric field. Interfacing PtSe₂ monolayer

with graphene breaks the symmetry due to the interfacial dipole and thus induces a Rashba splitting of those bands as can be seen from the spin textures in Fig. 6e and 6f. Indeed, the band splitting is found to be larger for the VB with an estimated Rashba parameter $\alpha_R \approx -195 \text{ meV}\cdot\text{\AA}$ and can be explained by its orbital character which is mainly contributed by the p-orbitals of Se whereas the CB is dominated by Pt d-orbitals. Despite the fact that Pt has larger spin-orbit strength, the Se atoms are positioned at the interface which makes their bands more sensitive to the interfacial dipole effect. Although often neglected in the transition metal systems owing to the reduced hole velocity in the VB, the first step in THz emission (Fig. 6e) most probably originates from IREE in this valence band where spin polarized hot holes are injected from CoFeB. However, it is difficult to estimate the fraction of hot holes reaching this band since the position of the Fermi level altered by CoFeB deposition is unknown. ISHE in multilayers PtSe₂, corresponding to the second step in THz emission (Fig. 6e), can be of extrinsic or intrinsic origin and further investigation would be required to identify its exact mechanism. Nevertheless, as shown in the Supp. Info., we already observe avoided band crossings in the VB of 3 ML PtSe₂ that are supposed to contribute to intrinsic ISHE.

III. CONCLUSION

In conclusion, we have realised large area and high quality 2D PtSe₂ on graphene by molecular beam epitaxy, on which in-situ grown CoFeB is sputtered to study THz SCC phenomena. By performing a careful and extensive characterization of PtSe₂ layers before and after CoFeB deposition, we find that the 2D material retains its structural and chemical properties. For SCC, we performed spintronic THz emission spectroscopy and find efficient THz emission from PtSe₂, whereas VSe₂ and WSe₂ give negligible signals owing to low SOC and 1H crystal symmetry, respectively. From the PtSe₂ heterostructures, we clearly demonstrate the magnetic origin of the THz signal and unveil the physical origin of the SCC through a PtSe₂ thickness dependence study. The emitted THz electric field as a function of the number of PtSe₂ monolayers exhibits a clear two-step behaviour, which reflects the transition from the IREE in semiconducting thin PtSe₂ (≤ 3 ML) to ISHE in thicker semimetallic PtSe₂ (> 3 ML). We also deduce the vertical spin diffusion length in PtSe₂ to be 2-3 nm and find that IREE is twice as efficient compared to ISHE for SCC. Our

conclusions are supported by first principles calculations showing the existence of Rashba SOC at the PtSe₂/Gr interface. The unique band structure flexibility of PtSe₂ makes it an ideal candidate as a THz spintronic 2D material and to further explore the underlying mechanisms and engineering of the SCC for THz emission.

IV. EXPERIMENTAL SECTION

Raman spectroscopy

For Raman measurements, we used a Renishaw INVIA 1 spectrometer with a green laser (532 nm) and a 1800 gr/mm grating. The microscope objective magnification was $\times 100$ and the numerical aperture 0.9. The laser power was $< 150 \mu\text{W}/\mu\text{m}^2$. All the spectra correspond to the average of at least three spectra recorded at different locations on the samples.

X-ray diffraction

The grazing incidence X-ray diffraction (GIXD) was done with a SmartLab Rigaku diffractometer equipped with a copper rotating anode beam tube ($K_\alpha=1.54 \text{ \AA}$) operating at 45 kV and 200 mA. Parallel in-plane collimators of 0.5° of resolution were used both on the source and detector sides. The out-of-plane XRD measurements were performed using a Panalytical Empyrean diffractometer operated at 35 kV and 50 mA, with a cobalt source, ($K_\alpha= 1.79 \text{ \AA}$). A PIXcel-3D detector allowed a resolution of 0.02° per pixel, in combination with a divergence slit of 0.125° . Both diffractometers are equipped with multilayer mirror on the incident beam and K_β filter on the diffracted beam.

Transmission electron microscopy

Scanning transmission electron microscopy (STEM) measurements were performed using a Cs-corrected FEI Themis at 200 kV. HAADF-STEM (high-angle annular dark field) images were acquired using a convergence angle of 20 mrad and collecting electrons scattered at angles higher than 60 mrad. STEM specimens were prepared by the focused ion beam (FIB) lift-out technique using a Zeiss Crossbeam 550. The sample was coated with protective carbon and platinum layers prior to the FIB cut.

X-ray photoemission spectroscopy

XPS was performed in situ using a Staib Instruments spectrometer. We used an aluminum anode with K_α emission operating at 300 W. The signal was optimized on the Se LMM Auger spectra at a binding energy of 184 eV. The C1s line was used to set the binding

energy scale.

V. ACKNOWLEDGEMENTS

The authors acknowledge the support from the European Union's Horizon 2020 research and innovation Programme under grant agreement No 881603 (Graphene Flagship), No 829061 (FET-OPEN NANOPOLY) and No 964735 (FET-OPEN EXTREME-IR). The French National Research Agency (ANR) is acknowledged for its support through the ANR-18-CE24-0007 MAGICVALLEY and ESR/EQUIPEX+ ANR-21-ESRE-0025 2D-MAG projects. The LANEF framework (No. ANR-10-LABX-0051) is acknowledged for its support with mutualized infrastructure.

-
- [1] Novoselov, K., Geim, A., Morozov, S., Jiang, D., Zhang, Y., Dubonos, S., Grigorieva, I. & A. A. Firsov Electric Field Effect in Atomically Thin Carbon Films. *Science*. **306**, 666-669 (2004).
 - [2] Novoselov, K., Geim, A., Morozov, S., Jiang, D., Katsnelson, M., Grigorieva, I., Dubonos, S. & Firsov, A. Two-dimensional gas of massless Dirac fermions in graphene. *Nature*. **438**, 197-200 (2005).
 - [3] Cao, Y., Fatemi, V., Fang, S., Watanabe, K., Taniguchi, T., Kaxiras, E. & Jarillo-Herrero, P. Unconventional superconductivity in magic-angle graphene superlattices. *Nature*. **556**, 43-50 (2018).
 - [4] Mak, K., Lee, C., Hone, J., Shan, J. & Heinz, T. Atomically Thin MoS₂: A New Direct-Gap Semiconductor. *Phys. Rev. Lett.* **105**, 136805 (2010).
 - [5] Cadiz, F., Courtade, E., Robert, C., Wang, G., Shen, Y., Cai, H., Taniguchi, T., Watanabe, K., Carrere, H., Lagarde, D., Manca, M., Amand, T., Renucci, P., Tongay, S., Marie, X. & Urbaszek, B. Excitonic Linewidth Approaching the Homogeneous Limit in MoS₂-Based van der Waals Heterostructures. *Phys. Rev. X*. **7**, 021026 (2017).
 - [6] Xiao, D., Liu, G., Feng, W., Xu, X. & Yao, W. Coupled Spin and Valley Physics in Monolayers of MoS₂ and Other Group-VI Dichalcogenides. *Phys. Rev. Lett.* **108**, 196802 (2012).

- [7] Sallen, G., Bouet, L., Marie, X., Wang, G., Zhu, C., Han, W., Lu, Y., Tan, P., Amand, T., Liu, B. & Urbaszek, B. Robust optical emission polarization in MoS₂ monolayers through selective valley excitation. *Phys. Rev. B*. **86**, 081301 (2012).
- [8] Mak, K., McGill, K., Park, J. & P. L. McEuen The valley Hall effect in MoS₂ transistors. *Science*. **344**, 1489-1492 (2014).
- [9] Dau, M., Vergnaud, C., Marty, A., Beigné, C., Gambarelli, S., Maurel, V., Journot, T., Hyot, B., Guillet, T., Grévin, B., Okuno, H. & Jamet, M. The valley Nernst effect in WSe₂. *Nature Communications*. **10**, 5796 (2019).
- [10] Benítez, L., Sierra, J., Savero Torres, W., Arrighi, A., Bonell, F., Costache, M. & Valenzuela, S. Strongly anisotropic spin relaxation in graphene–transition metal dichalcogenide heterostructures at room temperature. *Nature Physics*. **14**, 303-308 (2018).
- [11] Guimarães, M., Stiehl, G., MacNeill, D., Reynolds, N. & Ralph, D. Spin–Orbit Torques in NbSe₂/Permalloy Bilayers. *Nano Letters*. **18**, 1311-1316 (2018).
- [12] Zhao, Y., Qiao, J., Yu, Z., Yu, P., Xu, K., Lau, S., Zhou, W., Liu, Z., Wang, X., Ji, W. & Chai, Y. High-Electron-Mobility and Air-Stable 2D Layered PtSe₂ FETs. *Advanced Materials*. **29**, 1604230 (2017).
- [13] Bonell, F., Marty, A., Vergnaud, C., Consonni, V., Okuno, H., Ouerghi, A., Boukari, H. & Jamet, M. High carrier mobility in single-crystal PtSe₂ grown by molecular beam epitaxy on ZnO(0001). *2D Materials*. **9**, 015015 (2021).
- [14] Cao, B., Ye, Z., Yang, L., Gou, L. & Wang, Z. Recent progress in Van der Waals 2D PtSe₂. *Nanotechnology*. **32**, 412001 (2021).
- [15] Avsar, A., Cheon, C., Pizzochero, M., Tripathi, M., Ciarrocchi, A., Yazyev, O. & Kis, A. Probing magnetism in atomically thin semiconducting PtSe₂. *Nature Communications*. **11**, 4806 (2020).
- [16] Sant, R., Gay, M., Marty, A., Lisi, S., Harrabi, R., Vergnaud, C., Dau, M., Weng, X., Coraux, J., Gauthier, N., Renault, O., Renaud, G. & Jamet, M. Synthesis of epitaxial monolayer Janus SPtSe. *Npj 2D Materials And Applications*. **4**, 41 (2020).
- [17] Villaos, R., Crisostomo, C., Huang, Z., Huang, S., Padama, A., Albao, M., Lin, H. & Chuang, F. Thickness dependent electronic properties of Pt dichalcogenides. *Npj 2D Materials And Applications*. **3**, 2 (2019).

- [18] Yao, W., Wang, E., Huang, H., Deng, K., Yan, M., Zhang, K., Miyamoto, K., Okuda, T., Li, L., Wang, Y., Gao, H., Liu, C., Duan, W. & Zhou, S. Direct observation of spin-layer locking by local Rashba effect in monolayer semiconducting PtSe₂ film. *Nature Communications*. **8**, 14216 (2016).
- [19] Yan, M., Wang, E., Zhou, X., Zhang, G., Zhang, H., Zhang, K., Yao, W., Lu, N., Yang, S., Wu, S., Yoshikawa, T., Miyamoto, K., Okuda, T., Wu, Y., Yu, P., Duan, W. & Zhou, S. High quality atomically thin PtSe₂ films grown by molecular beam epitaxy. *2D Materials*. **4**, 045015 (2017).
- [20] Bangar, H., Kumar, A., Chowdhury, N., Mudgal, R., Gupta, P., Yadav, R., Das, S. & Muduli, P. Large Spin-To-Charge Conversion at the Two-Dimensional Interface of Transition-Metal Dichalcogenides and Permalloy. *ACS Applied Materials & Interfaces*. **14**, 41598-41604 (2022).
- [21] Seifert, T., Jaiswal, S., Martens, U., Hannegan, J., Braun, L., Maldonado, P., Freimuth, F., Kronenberg, A., Henrizi, J., Radu, I., Beaurepaire, E., Mokrousov, Y., Oppeneer, P., Jourdan, M., Jakob, G., Turchinovich, D., Hayden, L., Wolf, M., Münzenberg, M., Kläui, M. & Kampfrath, T. Efficient metallic spintronic emitters of ultrabroadband terahertz radiation. *Nature Photonics*. **10**, 483-488 (2016).
- [22] Rongione, E., Baringthon, L., She, D., Patriarche, G., Lebrun, R., Lemaître, A., Morassi, M., Reyren, N., Mićica, M., Mangeney, J., Tignon, J., Bertran, F., Dhillon, S., Le Fèvre, P., Jaffrès, H. & George, J. Spin-Momentum Locking and Ultrafast Spin-Charge Conversion in Ultrathin Epitaxial Bi_{1-x}Sb_x Topological Insulator. *Advanced Science*. **n/a**, 2301124.
- [23] Hawecker, J., Dang, T., Rongione, E., Boust, J., Collin, S., George, J., Drouhin, H., Laplace, Y., Grasset, R., Dong, J., Mangeney, J., Tignon, J., Jaffrès, H., Perfetti, L. & Dhillon, S. Spin Injection Efficiency at Metallic Interfaces Probed by THz Emission Spectroscopy. *Advanced Optical Materials*. **9**, 2100412 (2021).
- [24] Dang, T., Hawecker, J., Rongione, E., Baez Flores, G., To, D., Rojas-Sanchez, J., Nong, H., Mangeney, J., Tignon, J., Godel, F., Collin, S., Seneor, P., Bibes, M., Fert, A., Anane, M., George, J., Vila, L., Cosset-Cheneau, M., Dolfi, D., Lebrun, R., Bortolotti, P., Belashchenko, K., Dhillon, S. & Jaffrès, H. Ultrafast spin-currents and charge conversion at 3d-5d interfaces probed by time-domain terahertz spectroscopy. *Applied Physics Reviews*. **7**, 041409 (2020).
- [25] Cheng, L., Li, Z., Zhao, D. & Chia, E. Studying spin-charge conversion using terahertz pulses. *APL Materials*. **9**, 070902 (2021).

- [26] Cheng, L., Wang, X., Yang, W., Chai, J., Yang, M., Chen, M., Wu, Y., Chen, X., Chi, D., Goh, K., Zhu, J., Sun, H., Wang, S., Song, J., Battiato, M., Yang, H. & Chia, E. Far out-of-equilibrium spin populations trigger giant spin injection into atomically thin MoS₂. *Nature Physics*. **15**, 347-351 (2019).
- [27] Nádvořník, L., Gueckstock, O., Braun, L., Niu, C., Gräfe, J., Richter, G., Schütz, G., Takagi, H., Zeer, M., Seifert, T., Kubaščík, P., Pandeya, A., Anane, A., Yang, H., Bedoya-Pinto, A., Parkin, S., Wolf, M., Mokrousov, Y., Nakamura, H. & Kampfrath, T. Terahertz Spin-to-Charge Current Conversion in Stacks of Ferromagnets and the Transition-Metal Dichalcogenide NbSe₂. *Advanced Materials Interfaces*. **9**, 2201675 (2022).
- [28] Khusyainov, D., Guskov, A., Ovcharenko, S., Tiercelin, N., Preobrazhensky, V., Buryakov, A., Sigov, A. & Mishina, E. Increasing the Efficiency of a Spintronic THz Emitter Based on WSe₂/FeCo. *Materials*. **14** (2021).
- [29] Cong, K., Vetter, E., Yan, L., Li, Y., Zhang, Q., Xiong, Y., Qu, H., Schaller, R., Hoffmann, A., Kemper, A., Yao, Y., Wang, J., You, W., Wen, H., Zhang, W. & Sun, D. Coherent control of asymmetric spintronic terahertz emission from two-dimensional hybrid metal halides. *Nature Communications*. **12**, 5744 (2021).
- [30] Dau, M., Gay, M., Di Felice, D., Vergnaud, C., Marty, A., Beigné, C., Renaud, G., Renault, O., Mallet, P., Le Quang, T., Veuillen, J., Huder, L., Renard, V., Chapelier, C., Zamborlini, G., Jugovac, M., Feyer, V., Dappe, Y., Pochet, P. & Jamet, M. Beyond van der Waals Interaction: The Case of MoSe₂ Epitaxially Grown on Few-Layer Graphene. *ACS Nano*. **12**, 2319-2331 (2018).
- [31] Dau, M., Vergnaud, C., Gay, M., Alvarez, C., Marty, A., Beigné, C., Jalabert, D., Jacquot, J., Renault, O., Okuno, H. & Jamet, M. van der Waals epitaxy of Mn-doped MoSe₂ on mica. *APL Materials*. **7**, 051111 (2019).
- [32] Vergnaud, C., Dau, M., Grévin, B., Licitra, C., Marty, A., Okuno, H. & Jamet, M. New approach for the molecular beam epitaxy growth of scalable WSe₂ monolayers. *Nanotechnology*. **31**, 255602 (2020).
- [33] Vélez-Fort, E., Hallal, A., Sant, R., Guillet, T., Abd McKayumov, K., Marty, A., Vergnaud, C., Jacquot, J., Jalabert, D., Fujii, J., Vobornik, I., Rault, J., Brookes, N., Longo, D., Ohresser, P., Ouerghi, A., Veuillen, J., Mallet, P., Boukari, H., Okuno, H., Chshiev, M., Bonell, F. & Jamet, M. Ferromagnetism and Rashba Spin–Orbit Coupling in the Two-Dimensional (V,Pt)Se₂ Al-

- loy. *ACS Applied Electronic Materials*. **4**, 259-268 (2022).
- [34] Kumar, B., Baraket, M., Paillet, M., Huntzinger, J., Tiberj, A., Jansen, A., Vila, L., Cubuku, M., Vergnaud, C., Jamet, M., Lapertot, G., Rouchon, D., Zahab, A., Sauvajol, J., Dubois, L., Lefloch, F. & Duclairoir, F. Growth protocols and characterization of epitaxial graphene on SiC elaborated in a graphite enclosure. *Physica E: Low-dimensional Systems And Nanostructures*. **75** pp. 7-14 (2016).
- [35] Pallecchi, E., Lafont, F., Cavaliere, V., Schopfer, F., Maily, D., Poirier, W. & Ouerghi, A. High Electron Mobility in Epitaxial Graphene on 4H-SiC(0001) via post-growth annealing under hydrogen. *Scientific Reports*. **4**, 4558 (2014).
- [36] El Sachat, A., Xiao, P., Donadio, D., Bonell, F., Sledzinska, M., Marty, A., Vergnaud, C., Boukari, H., Jamet, M., Arregui, G., Chen, Z., Alzina, F., Sotomayor Torres, C. & Chavez-Angel, E. Effect of crystallinity and thickness on thermal transport in layered PtSe₂. *Npj 2D Materials And Applications*. **6**, 32 (2022).
- [37] Li, J., Kolekar, S., Ghorbani-Asl, M., Lehnert, T., Biskupek, J., Kaiser, U., Krashennnikov, A. & Batzill, M. Layer-Dependent Band Gaps of Platinum Dichalcogenides. *ACS Nano*. **15**, 13249-13259 (2021).
- [38] Zhang, L., Yang, T., Sahdan, M., Arramel, Xu, W., Xing, K., Feng, Y., Zhang, W., Wang, Z. & Wee, A. Precise Layer-Dependent Electronic Structure of MBE-Grown PtSe₂. *Advanced Electronic Materials*. **7**, 2100559 (2021).
- [39] Wu, X., Qiao, J., Liu, L., Shao, Y., Liu, Z., Li, L., Zhu, Z., Wang, C., Hu, Z., Ji, W., Wang, Y. & Gao, H. Shallowing interfacial carrier trap in transition metal dichalcogenide heterostructures with interlayer hybridization. *Nano Research*. **14**, 1390-1396 (2021).
- [40] Hibino, H., Kageshima, H., Kotsugi, M., Maeda, F., Guo, F. & Watanabe, Y. Dependence of electronic properties of epitaxial few-layer graphene on the number of layers investigated by photoelectron emission microscopy. *Phys. Rev. B*. **79**, 125437 (2009).
- [41] Liu, Y., Stradins, P. & Su-Huai Wei Van der Waals metal-semiconductor junction: Weak Fermi level pinning enables effective tuning of Schottky barrier. *Science Advances*. **2**, e1600069 (2016).
- [42] Filleter, T., Emtsev, K., Seyller, T. & Bennewitz, R. Local work function measurements of epitaxial graphene. *Applied Physics Letters*. **93**, 133117 (2008).

- [43] Quang, T., Cherkez, V., Nogajewski, K., Potemski, M., Dau, M., Jamet, M., Mallet, P. & Veullen, J. Scanning tunneling spectroscopy of van der Waals graphene/semiconductor interfaces: absence of Fermi level pinning. *2D Materials*. **4**, 035019 (2017).
- [44] Dappe, Y., Almadori, Y., Dau, M., Vergnaud, C., Jamet, M., Paillet, C., Journot, T., Hyot, B., Pochet, P. & Grévin, B. Charge transfers and charged defects in WSe₂/graphene-SiC interfaces. *Nanotechnology*. **31**, 255709 (2020).
- [45] Furuseth, S., Selte, K. & Kjekshus, A. Redetermined Crystal Structures of NiTe₂, PdTe₂, PtS₂, PtSe₂, and PtTe₂. *Acta Chemica Scandinavica*. **19**, 735-741 (1965).
- [46] Dau, M., Vergnaud, C., Marty, A., Beigné, C., Gambarelli, S., Maurel, V., Journot, T., Hyot, B., Guillet, T., Grévin, B., Okuno, H. & Jamet, M. The valley Nernst effect in WSe₂. *Nature Communications*. **10**, 5796 (2019).
- [47] Wang, M., Zhang, Y., Guo, L., Lv, M., Wang, P. & Wang, X. Spintronics Based Terahertz Sources. *Crystals*. **12** (2022).
- [48] Rongione, E., Fragkos, S., Baringthon, L., Hawecker, J., Xenogiannopoulou, E., Tsipas, P., Song, C., Mičica, M., Mangeney, J., Tignon, J., Boulier, T., Reyren, N., Lebrun, R., George, J., Le Fèvre, P., Dhillon, S., Dimoulas, A. & Jaffrès, H. Ultrafast Spin-Charge Conversion at SnBi₂Te₄/Co Topological Insulator Interfaces Probed by Terahertz Emission Spectroscopy. *Advanced Optical Materials*. **10**, 2102061 (2022).
- [49] Blöchl, P. Projector augmented-wave method. *Phys. Rev. B*. **50**, 17953-17979 (1994).
- [50] Kresse, G. & Hafner, J. Ab initio molecular dynamics for liquid metals. *Phys. Rev. B*. **47**, 558-561 (1993).
- [51] Kresse, G. & Furthmüller, J. Efficient iterative schemes for ab initio total-energy calculations using a plane-wave basis set. *Phys. Rev. B*. **54**, 11169-11186 (1996).
- [52] Kresse, G. & Furthmüller, J. Efficiency of ab-initio total energy calculations for metals and semiconductors using a plane-wave basis set. *Computational Materials Science*. **6**, 15-50 (1996).
- [53] Perdew, J., Burke, K. & Ernzerhof, M. Generalized Gradient Approximation Made Simple. *Phys. Rev. Lett.* **77**, 3865-3868 (1996).
- [54] Bučko, T., Hafner, J., Lebègue, S. & Ángyán, J. Improved Description of the Structure of Molecular and Layered Crystals: Ab Initio DFT Calculations with van der Waals Corrections. *The Journal Of Physical Chemistry A*. **114**, 11814-11824 (2010).

- [55] Herath, U., Tavadze, P., He, X., Bousquet, E., Singh, S., Muñoz, F. & Romero, A. PyProcar: A Python library for electronic structure pre/post-processing. *Computer Physics Communications*. **251** pp. 107080 (2020).
- [56] Sattar, S. & Schwingenschlögl, U. Electronic Properties of Graphene-PtSe₂ Contacts. *ACS Applied Materials & Interfaces*. **9**, 15809-15813 (2017)

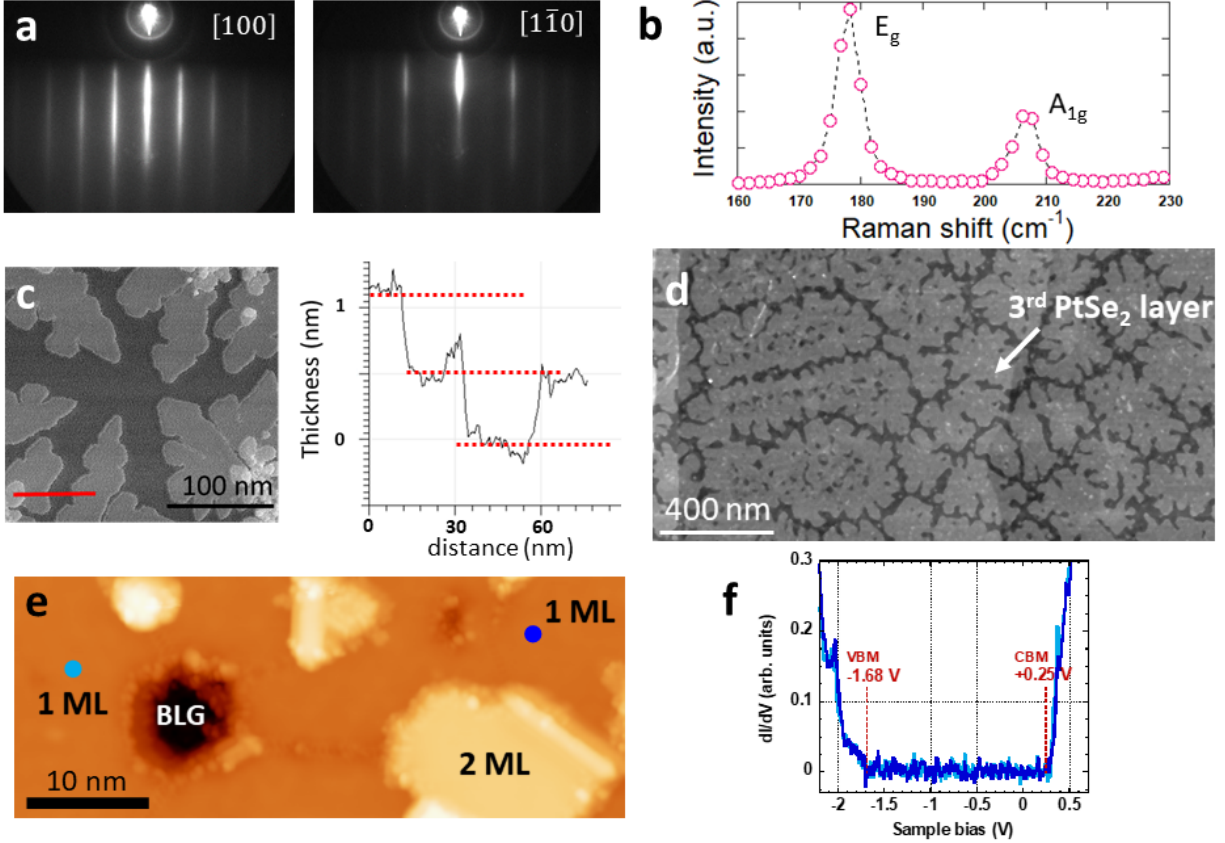


FIG. 1. (a) RHEED patterns of 10 ML PtSe₂ grown on Gr/SiC recorded along two different azimuths [100] and [110]. (b) Raman spectrum on the same sample. (c), (d) AFM images for <1 ML and 3 layers of PtSe₂ respectively. In (c), the height profile along the red solid line is shown on the right. (e) STM image showing a portion of uncovered bilayer graphene substrate (labelled BLG), a few domains of the monolayer 1T-PtSe₂ phase (labelled 1 ML) and an island of bilayer (labelled 2 ML). Image size: 50×20 nm², sample bias: +1.20 V. (f) STS spectra taken on two different 1 ML domains, at locations indicated by the blue dots of the same color in (e). The setpoint voltage (current) is +1.2 V (0.5 nA). The curves represent the lock-in signal. VBM, E_F and CBM correspond to the valence band maximum, the Fermi level and the conduction band minimum, respectively.

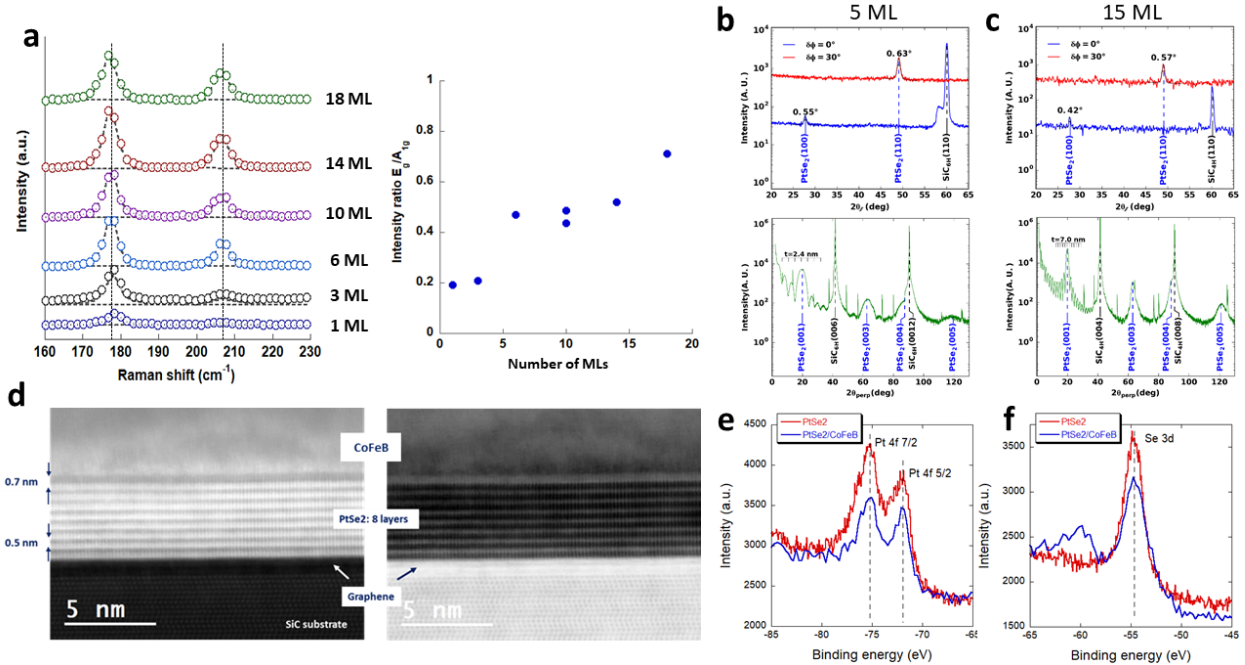


FIG. 2. (a) Raman spectra of Al/CoFeB/PtSe₂/Gr/SiC samples for different thicknesses of PtSe₂. The vertical dashed black lines correspond to the peak positions of Fig. 1b. On the right, the intensity ratio E_g/A_{1g} plotted as a function of the PtSe₂ thickness. (b), (c) Top: in-plane diffraction radial scans for 5 ML and 15 ML of PtSe₂ respectively. The scans were performed along 2 directions at 0° and 30° of the SiC(110) reciprocal direction. The full width at half maximum is shown above each PtSe₂ peak. The grazing incidence was set to an angle 0.5° and 0.6° respectively to maximize the intensity of the PtSe₂(110) peak. The thickness of the PtSe₂ layer and presence of CoFeB overlayer result in an optimum incidence angle slightly above the critical angle of the substrate. Bottom: specular $\theta/2\theta$ x-ray diffraction scans showing PtSe₂(00L) peaks, 2 major SiC peaks and many other weak intensity peaks related to the SiC polytype 4H or 6H. In addition, weak intensity peaks due to K_β radiation are not completely removed by the multilayer mirror and the K_β filter. At low angles, clearly visible fringes around the PtSe₂(001) Bragg peak show the quality of the PtSe₂ layer and allow to estimate its thickness reported above. (d) STEM/HAADF images in cross section of 8 ML of PtSe₂ covered with CoFeB in bright field (left) and dark field (right). Each PtSe₂ layer can be individually identified and a 0.7 nm gap is present at the CoFeB/PtSe₂ interface. (e), (f) XPS spectra of Pt 4f and Se 3d core levels respectively. Red (blue) before (after) CoFeB coverage.

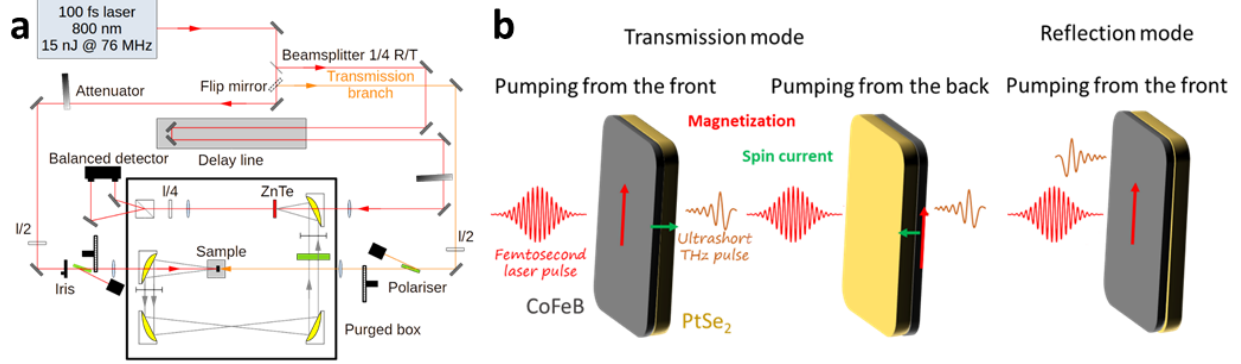


FIG. 3. (a) Schematics of the THz setup. (b) The 3 different measurement geometries: transmission mode with pumping from the front and the back sides and reflection mode. CoFeB is in grey and PtSe₂ in yellow. The red (green) arrow corresponds to the CoFeB magnetization (injected spin current).

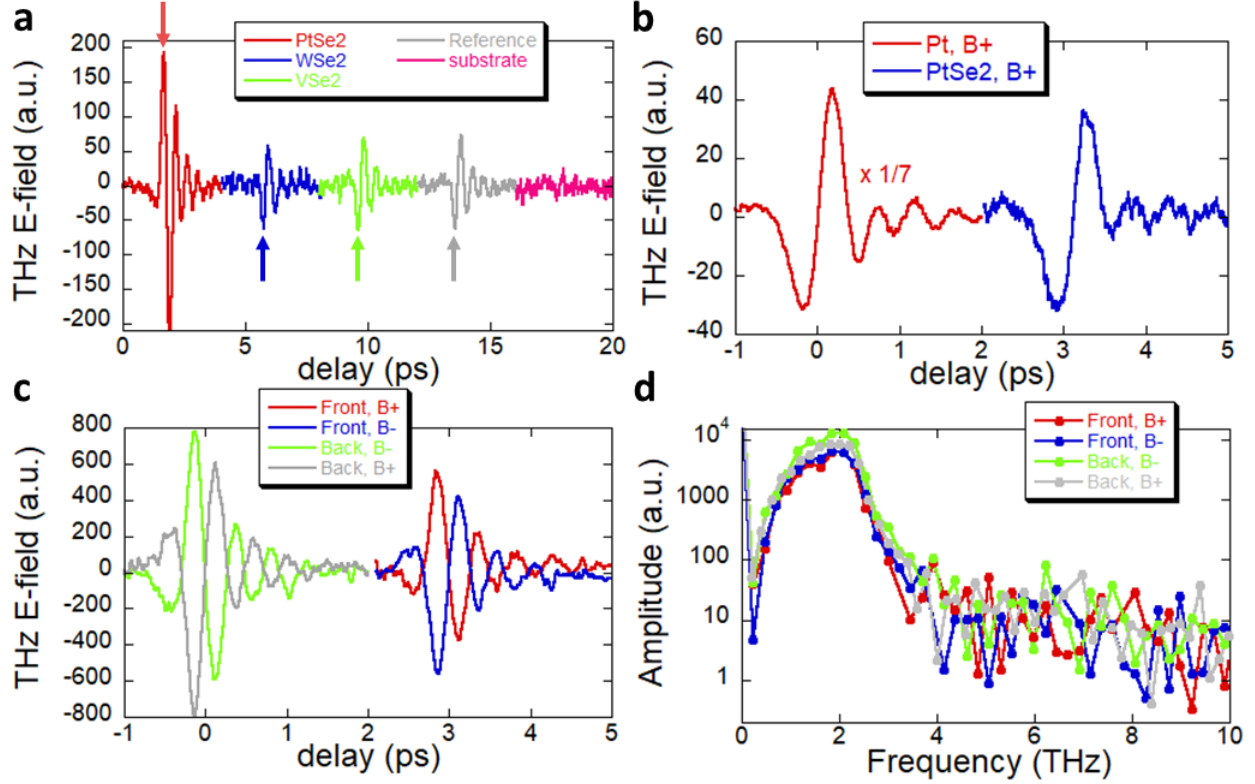


FIG. 4. (a) THz E-field emitted by CoFeB/10 ML PtSe₂ (red), CoFeB/10 ML WSe₂ (blue), CoFeB/10 ML VSe₂ (green), CoFeB/Gr reference sample (grey) and bare Gr/SiC substrate (pink). The arrows indicate the position of the first THz E-field peak: positive for PtSe₂ and negative for WSe₂, VSe₂ and reference sample. All the measurements were carried out in reflection mode with a 15 fs laser pulse and 0.1 mm ZnTe detector and with a fixed 20 mT (B+) applied magnetic field. (b) THz emission for 5 nm of Pt and 5 nm (10 ML) of PtSe₂ measured in the same conditions and magnetic field. They show the same sign but the Pt signal is 7 times larger than the one of PtSe₂. The measurements were carried out in transmission mode from the backside with a 100 fs laser pulse and a 2 mm ZnTe detector. (c) THz emission of 10 ML PtSe₂ measured in transmission mode with a 15 fs laser pulse and 1 mm ZnTe detector. The sample was pumped from the back (front) side with positive magnetic field in grey (red) and negative magnetic field in green (blue). (d) Fourier transform of the four previous spectra.

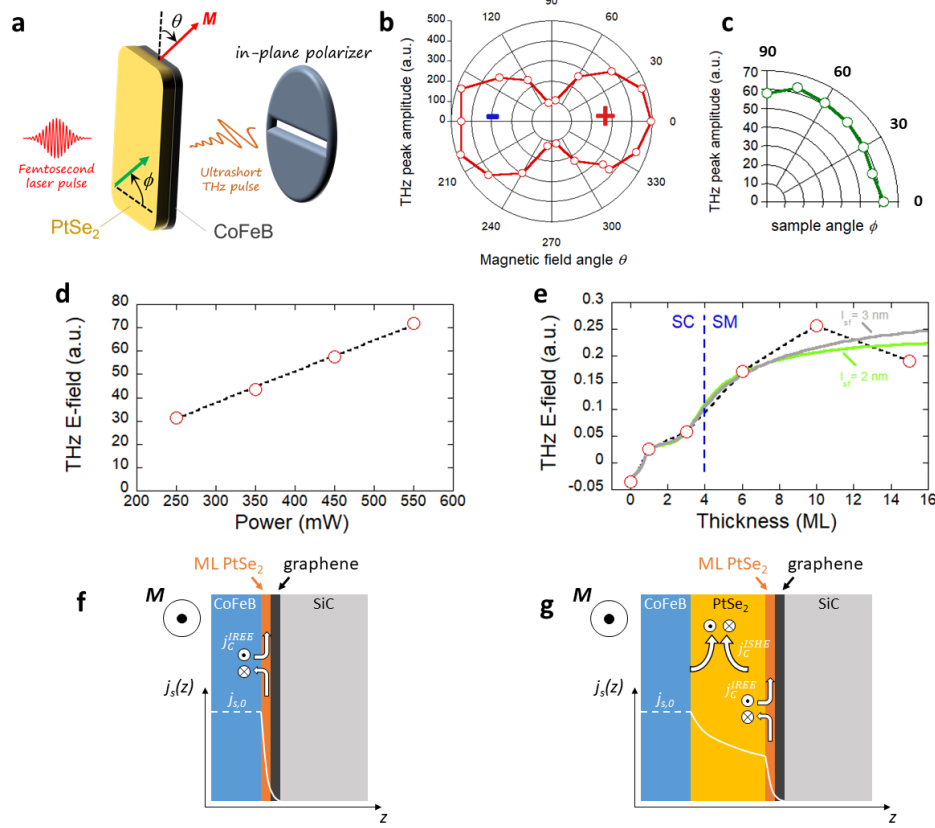


FIG. 5. (a) Geometry used to measure THz emission angular dependence. The polarizer selects only in-plane polarized THz waves. θ is the angle between the vertical axis and the applied magnetic field of 20 mT. The magnetization M of CoFeB is along the field direction because of its soft magnetic character. ϕ is the angle between the sample and horizontal axis. (b) θ dependence of the THz peak amplitude. The + and - signs correspond to the phase of the THz E-field. The sample was fixed and the measurements were performed in reflection mode with a laser pulse of 15 fs and a 0.1 mm ZnTe detector. (c) ϕ dependence of the THz peak amplitude. The magnetic field was fixed. (d) Laser power dependence of $\frac{E_{B+} + E_{B-}}{2}$ (red open circles). The measurements were performed in transmission pumped from the backside with a laser pulse of 100 fs and a 2 mm ZnTe detector. (e) Thickness dependence of $\frac{E_{B+} + E_{B-}}{2}$ (red open circles) after normalization by laser and THz absorption by PtSe₂ (see Supp. Info.). The measurements were performed in transmission pumped from the backside with a laser pulse of 100 fs and a 2 mm ZnTe detector. The grey (green) solid lines are fits to the experimental data using Eq. 1 and $l_{sf}=3$ nm ($l_{sf}=2$ nm). (f) and (g) Schematics of the SCC in PtSe₂ from one layer (IREE) to multilayers (IREE+ISHE) respectively. White curve: profile of $j_s(z)$. $j_s(0)$ is the effective spin current injected in PtSe₂ from optically pumped CoFeB.

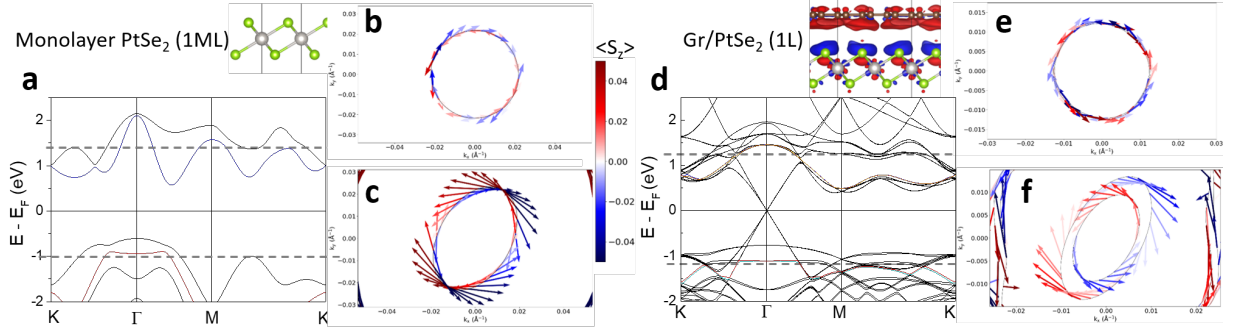


FIG. 6. Rashba effect at PtSe₂/Gr interface. (a) Band structure of a freestanding PtSe₂ monolayer calculated by including spin-orbit coupling. In the shown crystal structure, the grey (green) balls represent the Pt (Se) atoms, respectively. (b) Calculated two-dimensional spin textures for the blue CB band in (a) at an energy cut $E = E_F + 0.4$ eV corresponding to the black dashed line. (c) Spin textures for the red VB in (a) at an energy cut of $E = E_F - 1$ eV. The arrows in the spin texture plots represent the S_x and S_y spin projections while the colour code corresponds to the S_z component. (d) Calculated band structure of monolayer-PtSe₂/Gr heterostructure. The charge transfer occurring at the interface can be depicted on the crystal structure by red (blue) clouds corresponding to charge depletion (accumulation) taken at an isosurface value of $10^{-4} e/\text{\AA}^3$. (e, f) Spin textures in PtSe₂/Gr heterostructure calculated for the CB (at an energy cut $E = E_F + 1.25$ eV) and VB (at an energy cut $E = E_F - 1.1$ eV) chosen as in (b, c). The Rashba spin splitting is clearly visible in the VB.